sensors

MDPI

Article

A GRU-KAN Surrogate Model with Genetic Algorithm Uniform Sampling for Active Magnetic Bearings–Rotor Critical Speed Prediction

Jiahang Cui [1], Jianghong Li [1,2,*], Feichao Cai [1,3], Zhenmin Zhao [4] and Yuxi Liu [1]

[1] School of Power and Energy, Northwestern Polytechnical University, Xi'an 710129, China; cui275228896@mail.nwpu.edu.cn (J.C.); liuyuxi0318@163.com (Y.L.)
[2] Science and Technology on Altitude Simulation Laboratory, Mianyang 62100, China
[3] National Key Laboratory of Science and Technology on Advanced Light-Duty Gas-Turbine, Xi'an 710129, China
[4] National Elite Institute of Engineering, Northwestern Polytechnical University, Xi'an 710129, China; 2022160894@mail.nwpu.edu.cn
* Correspondence: jhli@nwpu.edu.cn

Abstract

With the development of active magnetic bearings (AMBs) toward higher speeds, understanding high-speed rotor dynamics has become a crucial focus in AMB research. Traditional finite element modeling (FEM) methods, however, are unable to rapidly and comprehensively uncover the complex interplay between controller parameters and dynamic behavior. To address this limitation, a surrogate modeling approach based on a hybrid gated recurrent unit–Kolmogorov–Arnold network (GRU-KAN) is introduced to mathematically capture the effects of coupled control gains on rotor dynamics. To enhance model generalization, a genetic algorithm-driven uniform design sampling strategy is also implemented. Comparative studies against support vector regression and Kriging surrogates indicate a higher coefficient of determination ($R^2 = 0.9887$) and lower residuals for the proposed approach. Experimental validation across multiple controller parameter combinations shows that the resulting machine learning surrogate predicts the critical speed with a mean absolute error of only 38.51 rpm and a mean absolute percentage error of 1.56×10^{-1}%, while requiring merely 1.14×10^{-4} s per evaluation—compared to 201 s for traditional FEM. These findings demonstrate the surrogate's efficiency, accuracy, and comprehensive predictive capabilities, offering an effective method for rapid critical speed estimation in AMB–rotor systems.

Keywords: AMB–rotor; dynamic model; surrogate model; GRU-KAN; critical speed

check for updates

Academic Editor: Xinqun Zhu

Received: 10 July 2025
Revised: 19 August 2025
Accepted: 10 September 2025
Published: 11 September 2025

Citation: Cui, J.; Li, J.; Cai, F.; Zhao, Z.; Liu, Y. A GRU-KAN Surrogate Model with Genetic Algorithm Uniform Sampling for Active Magnetic Bearings–Rotor Critical Speed Prediction. *Sensors* **2025**, *25*, 5680. https://doi.org/10.3390/s25185680

Copyright: © 2025 by the authors. Licensee MDPI, Basel, Switzerland. This article is an open access article distributed under the terms and conditions of the Creative Commons Attribution (CC BY) license (https://creativecommons.org/licenses/by/4.0/).

1. Introduction

1.1. Background

AMBs are widely employed in systems such as torque gyroscopes, flywheel energy storage devices, blowers, centrifugal compressors, and other electric engines [1]. Early AMB research focused on manufacturing, packaging, and topology design, yielding notable performance test results [2]. As an open-loop unstable nonlinear mechatronic system, the AMB–rotor assembly requires feedback control to ensure stable operation, while the influence of the rotor dynamics must not be neglected [3]. With recent advances in computational power, models have progressively evolved toward multidisciplinary and multiparameter

coupling [4,5], furnishing powerful theoretical tools for the more accurate characterization of dynamic behavior.

1.2. Literature Review

1.2.1. Dynamic Modeling Methods for AMB–Rotors

Many researchers have investigated AMB–rotor dynamic modeling. In [6], FEM theory was used to derive MATLAB 2021a-computed and workbench-simulated dynamic models of both rigid and flexible AMB–rotors supported by AMBs, comparing modal frequencies and mode shapes under varying equivalent stiffness; the study showed that tuning AMBs' stiffness shifts natural frequencies and thus mitigates vibration. In [7,8], an algorithm for the synchronous identification of rotor unbalance and residual AMB parameters was proposed. This algorithm was developed based on Timoshenko beam theory, the finite element method, and a misalignment approach. The efficacy of the proposed algorithm was demonstrated through experimental testing, which yielded enhanced diagnostic accuracy and robustness. In [9], the design, construction, and modeling of a flexible rotor AMB test rig were detailed: by integrating conventional rotor dynamics analysis, FEM, and experimental validation, a comprehensive system model was established, proving that precise modeling coupled with model-based controller design enables the effective control of flexible rotors. In [10], a nonlinear dynamic model coupling the AMB and backup bearing was developed, systematically incorporating contact stiffness, sliding/rolling friction, aerodynamic damping, eddy current losses, and rotor geometric irregularity. This provided a high-fidelity description of the transient dynamics during rotor delevitation. In [11], the dynamic stiffness of radial AMBs in a magnetic-suspension molecular pump was analyzed and measured via combined frequency- and time-domain experiments, yielding detailed insights into bearing dynamic characteristics. In [12], a disturbance compensation control strategy for rotational-speed standard devices using an AMB force compensation system was proposed: by analyzing rotor unbalance dynamics and linearizing and decoupling the AMB force model across radial degrees of freedom, a PI-based force feedback controller was designed and validated on a semi-physical simulation platform, demonstrating the effective suppression of static, step, and synchronous vibration disturbances. In [13], the state space-based dynamic modeling and μ-synthesis control of flexible rotors and AMBs were presented and experimentally validated. In [14], a dynamic model based on radial and tilting motions was developed; simulations indicated that increasing angular acceleration markedly reduced the vibration amplitude at the radial critical speed, enabling an AMB–motor to traverse this critical speed without additional damping. In [15], building on a rotor dynamic model with incorporated gyroscopic effects, a fractional-order PID controller was formulated and optimized via particle swarm optimization to tune both the fractional orders and gain coefficients concurrently, achieving pole placement that markedly extended the stability margins and enhanced the dynamic response under high-speed operation.

Despite advances in single-physics rotor modeling, comprehensive analysis techniques for multidisciplinary and multiparameter coupled models remain relatively underdeveloped, particularly with respect to the impact of control parameter coupling on dynamic performance. In addition, the significant computational cost of parameter coupling analysis has not been adequately addressed.

1.2.2. Surrogate Model Methods

Surrogate models offer an effective route to study how control systems influence dynamic performance by rapidly constructing high-fidelity mappings between input variables and output responses [16–18], which endows them with unique advantages in rotor dynamics parameter identification. In [19], a hybrid surrogate model combining Kriging

and Polynomial Chaos Expansion (PCE) was developed to relate crack parameters to rotor system dynamic responses, enabling an analysis of how parameter variations shape the response surface. In [20], simulated annealing enhanced particle swarm-optimized support vector regression (SVR) surrogate models and improved the high-speed spindle thermal displacement prediction accuracy while reducing the computational complexity. In [21], a KAN was applied to system dynamics prediction; the results showed superior accuracy in forecasting the rotor angular frequency and identifying system uncertainty parameters with a smaller network scale than conventional machine learning methods, demonstrating the KAN's potential for the efficient, precise modeling of complex rotor systems. In [22], a particle swarm optimization method based on a mutation surrogate model was proposed for high-dimensional complex problems, using an initial sample selection strategy to build globally representative surrogate models. In [23], Latin hypercube sampling (LHS) was optimized to enhance surrogate models' exploration and exploitation performance, with a staged sample selection strategy that improved the global fidelity and accuracy under limited sample sizes.

Collectively, prior studies indicate that surrogate models have advanced mechatronic system modeling and prediction through global sample selection strategies and modern machine learning techniques, thereby supporting improved model fidelity. However, conventional surrogates remain susceptible to overfitting when the training set is sparse or unevenly distributed, and their robustness and accuracy are intrinsically constrained by the coverage of the sampled design space. In particular, when the available data are limited, Latin hypercube sampling may preserve marginal uniformity yet inadequately capture the response surface curvature and higher-order interactions [24], which can lead to reduced generalization.

1.3. Contributions

Therefore, this paper analyzes the influence of control parameters on dynamic models and proposes a GRU-KAN model based on a genetic algorithm uniform design (GAUD), comparing and analyzing it against SVR and Kriging models to investigate in depth the coupling between control parameters and the critical speed. We also introduce a novel method for the prediction of the critical speed of the AMB–rotor. The main contributions of this paper are as follows:

1. An evolutionary uniform design guided by a composite discrepancy metric is proposed. The scheme balances space filling with factor coupling and yields representative training sets suited to control–dynamics analysis.
2. A surrogate that combines gated recurrent units with a Kolmogorov–Arnold network is formulated to capture nonlinear interactions between controller parameters and rotor dynamics. In conjunction with the GAUD, this approach improves the data efficiency and predication capacity relative to conventional surrogates and clarifies controller–plant interactions.
3. The integrated GRU-KAN-UD workflow replaces repeated finite element simulations with rapid surrogate evaluation, enabling fast parametric exploration and early-stage design studies, thereby lowering the computational burden without compromising modeling fidelity.

The remainder of this manuscript is organized as follows. Section 2 formulates the AMB–rotor dynamic model. Section 3 details the GAUD design and GRU-KAN surrogate methodology. Section 4 presents the numerical and experimental results. Finally, Section 5 summarizes our findings.

2. AMB System Model

The AMB–rotor system is a prototypical, inherently unstable system. Therefore, unlike conventional rotor dynamics, the modeling and dynamic analysis of AMB–rotors primarily focus on control issues. The controlled plant includes not only the rotor structure but also displacement-sensing elements and power amplification units. To analyze and study the dynamics of the AMB–rotor, a dynamic model of the AMB system is first established. Figure 1 shows the five-degree-of-freedom configuration of the AMB–rotor. The structural parameters of the AMB and rotor are listed in Tables 1 and 2.

Table 1. Basic parameters of the radial AMB.

Parameter	Value
Bias current (A)	1.4
Number of coil turns	171
Pole area (mm^2)	742
One side air gap (mm)	0.8

Table 2. Basic parameters of the AMB–rotor.

Parameter	Variable	Value
Rotor mass (kg)	m	4.3
Total rotor length (mm)	l	502
Distance between radial AMB centers (mm)	l_1	192
Distance between end sensor centers (mm)	l_s	296
Right AMB to thrust disk distance (mm)	l_a	287.5
Left AMB to thrust disk distance (mm)	l_b	95.5

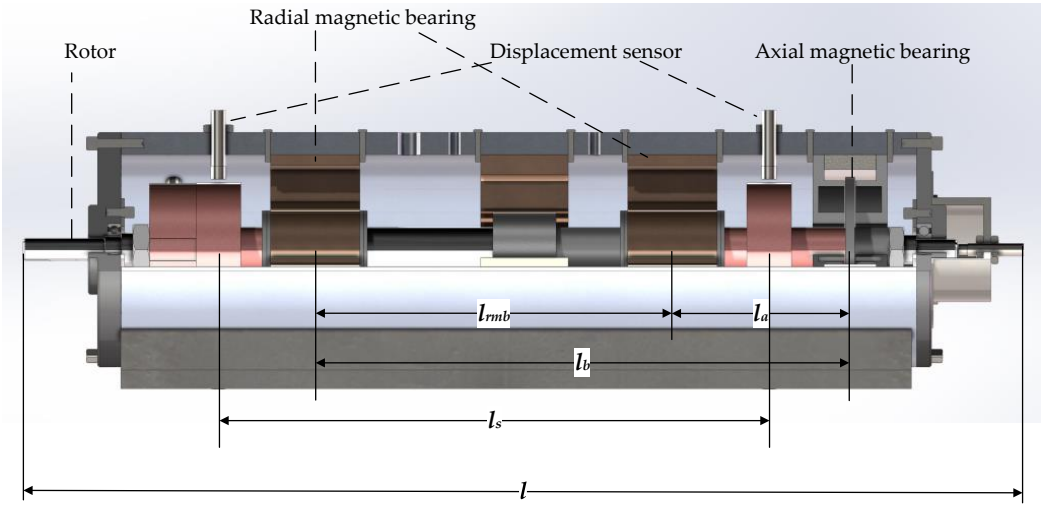


Figure 1. Structure diagram of AMB system.

2.1. Construction of the AMB–Rotor Dynamic Model

The dynamic equation of the AMB system can be written as

$$m\ddot{x} + c_e\dot{x} + k_e x = f \tag{1}$$

where m is the rotor mass, x the displacement, f the force acting on the rotor, c_e the equivalent damping coefficient, and k_e the equivalent stiffness coefficient.

Taking the Laplace transform of Equation (1) under zero initial conditions yields the frequency-domain transfer function (with $s = j\omega$)

$$\frac{X(j\omega)}{F(j\omega)} = \frac{1}{-m\omega^2 + k_e + c_e j\omega} \tag{2}$$

where s denotes the Laplace variable, $j = \sqrt{-1}$ is the imaginary unit, and ω is the angular frequency.

In this paper, an eddy current sensor is selected as the displacement sensor due to its simple structure, compact size, and high sensitivity. Its transfer function is

$$G_s(s) = A_s \tag{3}$$

where A_s denotes the sensor gain.

Within the frequency response range, the power amplifier can be modeled as a first-order inertial element:

$$G_a(s) = \frac{A_a}{T_a s + 1} \tag{4}$$

where A_a is the amplifier gain and T_a its time constant.

The support characteristics of the AMBs are principally determined by the control system. Thus, an analysis of stiffness and damping must be carried out under a given control strategy. Different controller parameters or algorithms yield distinct dynamic support properties. The closed-loop transfer function in the frequency domain is given in [25]:

$$\frac{X(j\omega)}{F(j\omega)} = \frac{1}{-m\omega^2 + k_{xx} + k_{ix} G_s(j\omega) G_a(j\omega) G_c(j\omega)} \tag{5}$$

where k_{xx} is the displacement–stiffness coefficient and k_{ix} the current–stiffness coefficient, and $G_c(j\omega)$ denotes the controller transfer function.

The electromagnetic stiffness and damping coefficients are defined by

$$\begin{cases} k_{xx} = -\frac{\mu_0 n^2 A I_0^2}{2x_0^3} \\ k_{ix} = \frac{\mu_0 n^2 A I_0}{2x_0^2} \end{cases} \tag{6}$$

with μ_0 being the permeability of free space, n the coil turns, A the pole area, I_0 the bias current, and x_0 the one-side air gap.

By combining Equations (2) and (5), substituting Equations (3) and (4), and applying the incomplete differential PID algorithm, the expression for the dynamic support characteristics is obtained:

$$\begin{cases} k_e = k_{xx} + k_{ix}\ \mathrm{Re}\{G_c(s)\, G_s(s)\, G_a(s)\} \\ \quad = k_{xx} + k_{ix}\ \mathrm{Re}\left\{ \left(K_p + \frac{K_i}{s} + K_d \frac{s}{1 + T_d s} \right) A_s \frac{A_a}{1 + T_a s} \right\}, \\ c_e = \frac{k_{ix}}{\omega}\ \mathrm{Im}\{G_c(s)\, G_s(s)\, G_a(s)\} \\ \quad = \frac{k_{ix}}{\omega}\ \mathrm{Im}\left\{ \left(K_p + \frac{K_i}{s} + K_d \frac{s}{1 + T_d s} \right) A_s \frac{A_a}{1 + T_a s} \right\}. \end{cases} \tag{7}$$

where K_p, K_i, K_d, and T_d are the proportional, integral, derivative, and incomplete differential gains of the PID controller; $\mathrm{Re}\{\cdot\}$ and $\mathrm{Im}\{\cdot\}$ denote the real and imaginary parts of a transfer function, respectively.

Based on these equivalent stiffness and damping definitions, FEM was performed in Ansys Workbench. A nominal mesh size of 5 mm was used, yielding 92,442 nodes and 26,114 elements after meshing. Boundary conditions reflect the five-DOF configuration: the AMB supports were modeled as spring connections located at the bearing stations. Using the Routh stability criterion, parameters were chosen as $K_p = 2000$, $K_i = 0.1$, $K_d = 20$, $T_d = 1 \times 10^{-4}$ and $I_0 = 1.4$ A, resulting in equivalent stiffness of 6.23×10^6 N/m and damping of 4.33×10^4 N·s/m. Gyroscopic effects were enabled for rotational speed sweeps to generate the Campbell diagram in Figure 2. As the speed increases, gyroscopic effects split the rotor's characteristic frequencies: the forward whirl rises, while the backward whirl falls, yielding a first critical speed of 24,870.54 rpm.

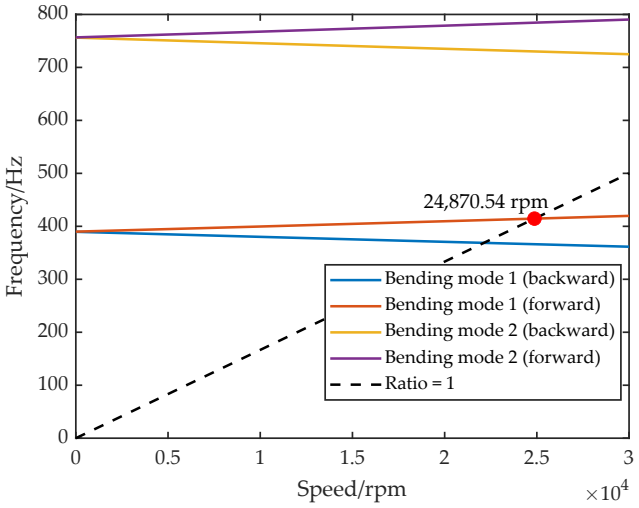


Figure 2. Campbell diagram of AMB–rotor.

2.2. *Effects of Individual Control Parameters on Critical Speed*

Based on the FEM, the influence of each single control parameter (proportional gain K_p, integral gain K_i, derivative gain K_d, incomplete differential gain T_d, and bias current I_0) on the AMB–rotor's critical speed was investigated. Each parameter was divided into ten equally spaced levels over its range (Table 3), while the other parameters were held at their mean values. FEM yielded the normalized first-order critical speed curves versus each parameter, as shown in Figure 3. The analysis indicates that increasing K_p significantly lowers the first critical speed; similarly, increases in K_d and I_0 also reduce it, albeit with a more gradual trend than for K_p. By contrast, variations in K_i and T_d have negligible effects on the critical speed.

Table 3. Ranges of control parameters.

Control Parameter	Range
K_p	[2000, 20,000]
K_i	[0.01, 0.1]
K_d	[8, 20]
T_d	$[5 \times 10^{-5}, 1 \times 10^{-4}]$
I_0 (A)	[0.8, 2]

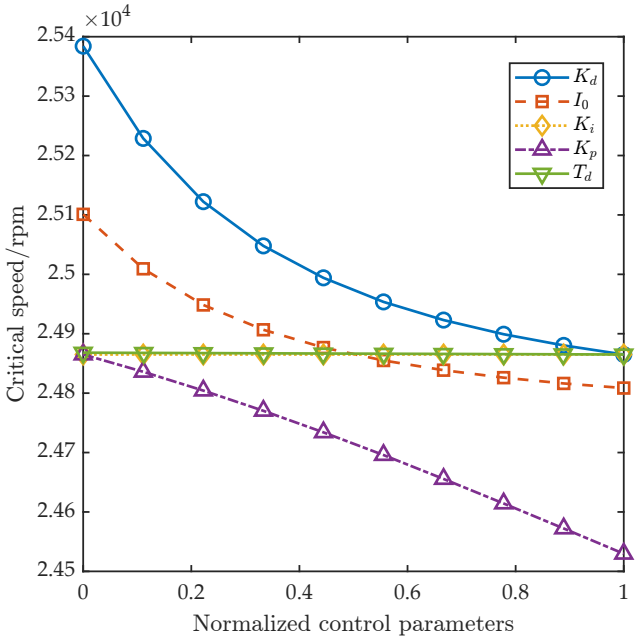


Figure 3. The influence of the control parameters on the dynamic characteristics of the AMB–rotor.

3. Surrogate Modeling of Control Parameters Versus Critical Speed

The direct sensitivity analysis of the control parameters is challenging due to the high dimensionality, strong parameter coupling, and substantial computation time. Surrogate models offer an efficient alternative, enabling the rapid evaluation of multivariable effects with significantly reduced complexity [26].

In this paper, we build a surrogate that maps the five control parameters (K_p, K_i, K_d, I_0, T_d) to the first critical speed. All FEM and surrogate model training was performed on a workstation with an Intel i9-9900 CPU (INTEL CHINA Co. Ltd., Shanghai, China) and 64 GB RAM (Shenzhen Kingbank Technology Co. Ltd., Shenzhen, China).

3.1. Surrogate Model Framework

The surrogate model construction follows two primary steps: the selection of initial samples and model training [27].

3.1.1. Uniform Design Sampling

Traditional uniform design can produce anisotropic samples in high-dimensional spaces [28], while Latin hypercube sampling may miss the response surface curvature [24]. We introduce a genetic algorithm-enhanced uniform design (GAUD) to generate more representative samples [29]. The flowchart of GAUD can be seen in Figure 4.

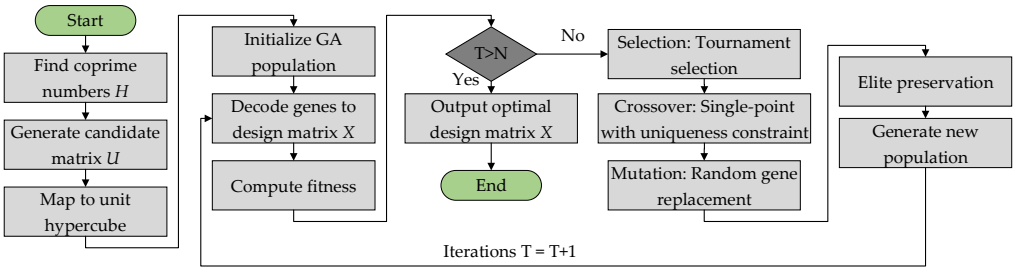


Figure 4. The flowchart of GAUD.

For n experiments, compute the set of integers coprime to n,

$$H = \{h_1, h_2, \ldots, h_m\}, \quad m = \phi(n), \tag{8}$$

where $\phi(n)$ is Euler's totient function. Form an $n \times m$ candidate matrix $U = [u_{ij}]$,

$$u_{ij} \;=\; i \cdot h_j \bmod n, \qquad i = 1, \ldots, n,\ j = 1, \ldots, m. \tag{9}$$

Map each entry to the midpoint of $(0, 1)$,

$$x_{ij} \;=\; \frac{u_{ij} + 0.5}{n}, \quad x_{ij} \in (0, 1), \tag{10}$$

yielding m columns of factor levels. These samples initialize the genetic algorithm, guided by a composite bias measure that adapts through fitness-driven iterations to capture both sample diversity and parameter coupling.

The algorithm minimizes the mixed bias measure $\mathrm{MD}^2(x)$,

$$\min_{x \in X_{n \times n_f}} \mathrm{MD}^2(x), \tag{11}$$

where n_f is the number of factors and $X_{n \times n_f}$ the sample table. The measure is defined as

$$\begin{aligned} MD^2(x) = &\left(\frac{19}{12}\right)^{n_f} - \\ &\frac{2}{n}\sum_{i=1}^{n}\prod_{j=1}^{n_f}\left(\frac{5}{3} - \frac{1}{4}\left|x_{ij} - \frac{1}{2}\right| - \frac{1}{4}\left|x_{ij} - \frac{1}{2}\right|^2\right) + \\ &\frac{1}{n^2}\sum_{i=1}^{n}\sum_{k=1}^{n}\prod_{j=1}^{n_f}\left(\begin{array}{l}\frac{15}{8} - \frac{1}{4}|x_{ij} - \frac{1}{2}| - \frac{1}{4}|x_{kj} - \frac{1}{2}| \\ -\frac{3}{4}|x_{ij} - x_{kj}| + \frac{1}{2}|x_{ij} - x_{kj}|^2\end{array}\right) \end{aligned} \tag{12}$$

3.1.2. Support Vector Regression

SVR allows an error tolerance zone ε_s, penalizing only deviations beyond this threshold [30]. The prediction function is

$$f(x) = v^T \phi(x) + b \tag{13}$$

where $\phi(x)$ is the nonlinear mapping function, v the weight vector, and b the bias term. SVR minimizes the regularized risk

$$\min_{v, b, \{\xi_i, \hat{\xi}_i\}} \frac{1}{2}\|v\|^2 + C\sum_{i=1}^{m}\left(\xi_i + \hat{\xi}_i\right) \tag{14}$$

subject to

$$\begin{cases} y_i - f(x_i) \le \varepsilon_s + \xi_i, \\ f(x_i) - y_i \le \varepsilon_s + \hat{\xi}_i, \\ \xi_i,\ \hat{\xi}_i \ge 0, \end{cases} \tag{15}$$

where $C > 0$ is a regularization parameter balancing model complexity and tolerance, and $\xi_i, \hat{\xi}_i$ are slack variables. By applying Lagrange duality, the solution takes the form

$$f(x) = \sum_{i=1}^{m}\left(\alpha_i - \hat{\alpha}_i\right) K(x, x_i) + b \tag{16}$$

where $\alpha_i, \hat{\alpha}_i$ are Lagrange multipliers and $K(\cdot,\cdot)$ is the kernel function mapping inputs to a high-dimensional feature space.

3.1.3. Kriging

Kriging represents the response surface $G(\Theta)$ as the combination of a regression term and a Gaussian process [31]

$$G(\Theta) = \sum_{i=1}^{p} \beta_i w_i(\Theta) + z(\Theta) \tag{17}$$

where $w_i(\Theta)$ denotes the chosen basis functions, β_i denotes the regression coefficients fitted to the data, and $z(\Theta) \sim \mathcal{N}(0, \sigma^2)$ is a zero-mean Gaussian process capturing local deviations. The covariance between two sample points $\Theta^{(i)}$ and $\Theta^{(j)}$ is [32]

$$Cov[z(\theta^{(i)}), z(\theta^{(j)})] = \sigma^2[R(\theta^{(i)}, \theta^{(j)})] \tag{18}$$

where the matrix R encodes correlations critical to the prediction accuracy. The regression coefficients and process variance are estimated by

$$\begin{cases} \hat{\beta} = \left(W^{\mathrm{T}} R^{-1} W\right)^{-1} W^{\mathrm{T}} R^{-1} m_k \\ \hat{\sigma}^2 = (m_k - W\hat{\beta})^{\mathrm{T}} R^{-1} (m_k - W\hat{\beta}) / N_T \end{cases} \tag{19}$$

with m_k being the vector of the observed responses and W the $N_T \times p$ regression matrix. The hyperparameters $\boldsymbol{\varepsilon} = [\varepsilon_1, \ldots, \varepsilon_b]^T$ governing the covariance function are obtained by maximizing the log-likelihood:

$$maxF(\varepsilon) = -\frac{N_T ln\left(\hat{\sigma}^2\right) + ln|\mathrm{R}|}{2} (\varepsilon \geqslant 0) \tag{20}$$

3.1.4. Gated Recurrent Unit–Kolmogorov–Arnold Network

The GRU-KAN architecture combines gated recurrent units with Kolmogorov–Arnold networks to leverage the GRU's temporal modeling and the KAN's universal approximation, improving both the accuracy and interpretability [33]. Its structure is shown in Figure 5.

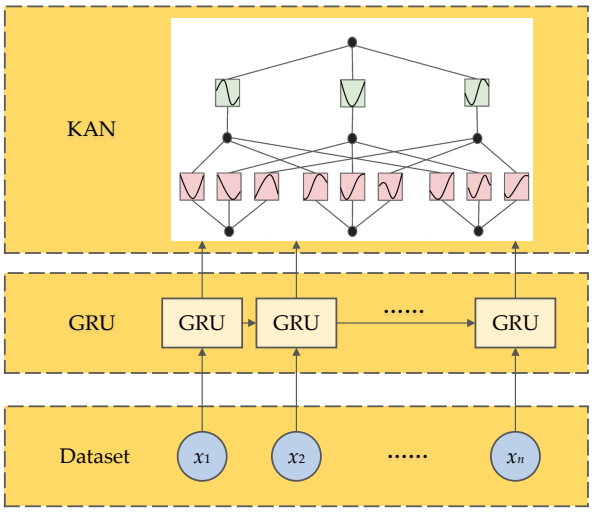


Figure 5. GRU-KAN network structure.

The GRU core updates are

$$\begin{cases} r_t = \sigma\left(W_r x_t + U_r h_{t-1} + b_r\right) \\ z_t = \sigma\left(W_z x_t + U_z h_{t-1} + b_z\right) \\ \tilde{h}_t = \tanh\left(W_h x_t + U_h (r_t \odot h_{t-1}) + b_h\right) \\ h_t = (1 - z_t) \odot h_{t-1} + z_t \odot \tilde{h}_t \end{cases} \tag{21}$$

where z_t and r_t are the reset and update gates; $\tilde{h}_t$ is the candidate state; h_t is the hidden state; $\sigma(\cdot)$ is the sigmoid function; $\tanh(\cdot)$ is the hyperbolic tangent; and W_*, U_*, b_* are the weight and bias parameters.

The KAN decomposes a multivariate function into univariate components

$$f(x_1, x_2, \ldots, x_n) = \sum_{q=1}^{2n+1} \phi_q \left(\sum_{p=1}^{n} \psi_{p,q}(x_p) \right) \tag{22}$$

where both $\phi_q(\cdot)$ and $\psi_{p,q}(\cdot)$ are one-dimensional continuous functions.

$$\mathbf{x}^{(l+1)} = \Phi^{(l)}\left(\mathbf{x}^{(l)}\right), \tag{23}$$

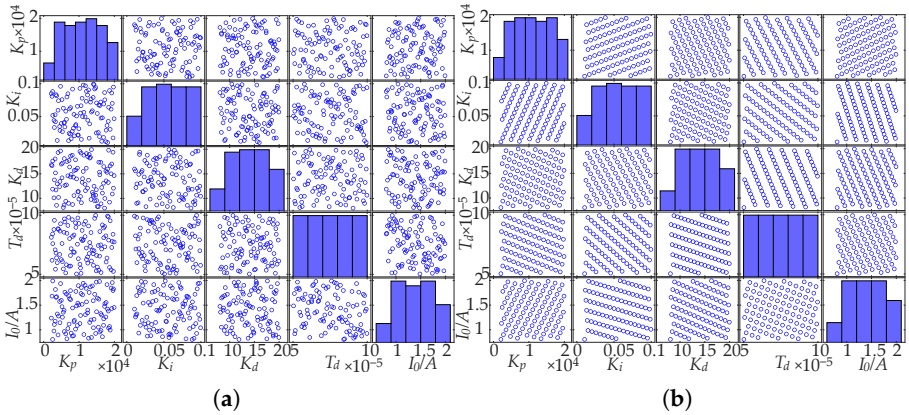
with

$$\Phi^{(l)} = \begin{pmatrix} \phi_{1,1}^{(l)}(\cdot) & \phi_{1,2}^{(l)}(\cdot) & \cdots & \phi_{1,n_l}^{(l)}(\cdot) \\ \phi_{2,1}^{(l)}(\cdot) & \phi_{2,2}^{(l)}(\cdot) & \cdots & \phi_{2,n_l}^{(l)}(\cdot) \\ \vdots & \vdots & \ddots & \vdots \\ \phi_{n_{l+1},1}^{(l)}(\cdot) & \phi_{n_{l+1},2}^{(l)}(\cdot) & \cdots & \phi_{n_{l+1},n_l}^{(l)}(\cdot) \end{pmatrix} \tag{24}$$

where n_l is the number of units in layer l, $x_i^{(l)}$ is the projection vector for unit i, and $\phi_{i,j}^{(l)}(\cdot)$ is the univariate activation function applied to its input.

3.2. Model Result Analysis

At $n = 100$ and $n_f = 5$, the initial samples generated by LHS and GAUD are shown in Figure 6. For the GAUD sampling procedure, the population size is set to 30 and the number of iterations to 200. The convergence behavior under these settings is illustrated in Figure 7. Using the mixed bias measure from Equation (12), GAUD achieves $\mathrm{MD}^2(x) = 0.0036$, significantly lower than LHS's 0.012, indicating a more uniform sample space.



(**a**) (**b**)

Figure 6. Sample scatter plots of (**a**) LHS and (**b**) GAUD.

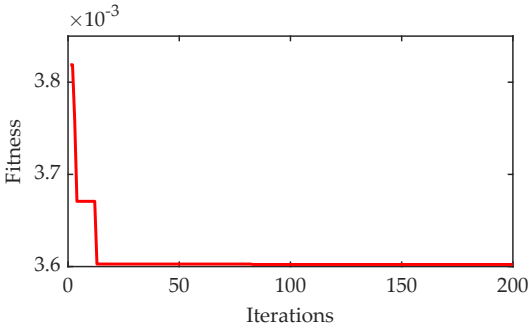


Figure 7. Convergence curve of GAUD.

To demonstrate the feasibility and advantages of the GRU-KAN model built on GAUD (GRU-KAN-UD), we compare five mappings from the control parameters to the critical speed: GRU-KAN-LHS, Kriging-UD, Kriging-LHS, SVR-UD, and SVR-LHS. All surrogate inputs are min–max normalized to $[0, 1]$. The hyperparameters for GRU-KAN, SVR, and Kriging are tuned via Bayesian optimization with five-fold cross-validation. The search spaces are summarized in Table 4.

The residuals for the first critical speed are plotted in Figure 8. Compared with LHS sampling, Kriging-UD and GRU-KAN-UD maintain high confidence across both low and high critical speeds, confirming that GAUD yields a broader yet accurate sample space.

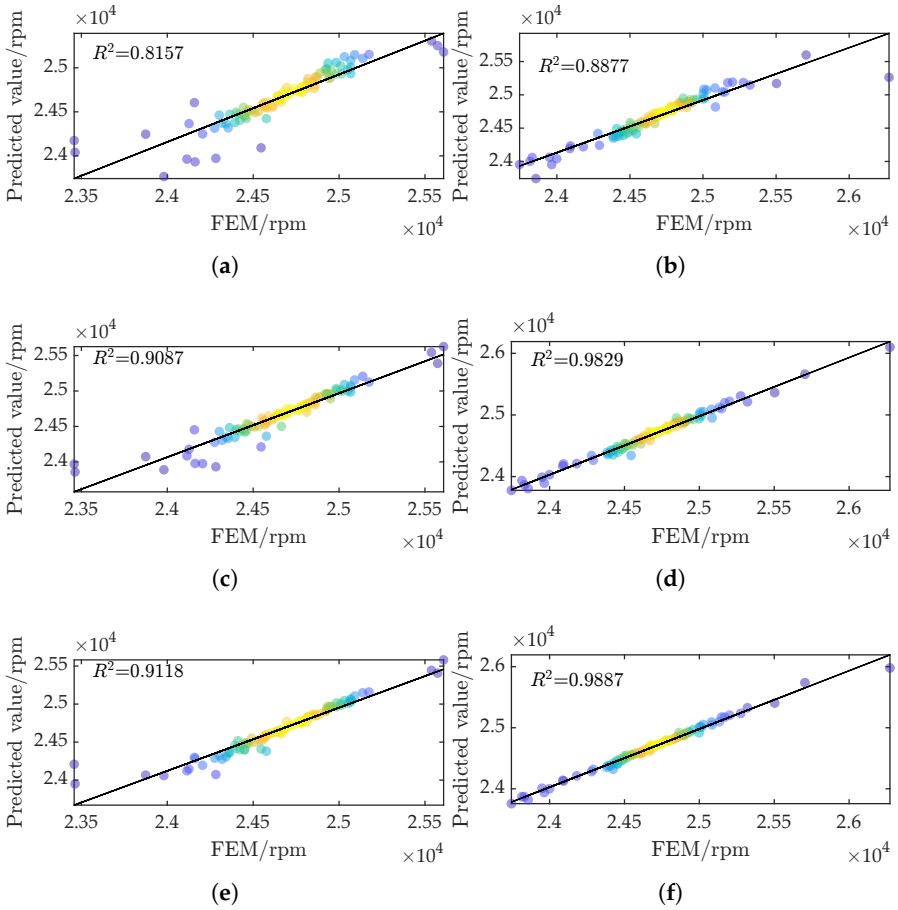


Figure 8. Comparison of residuals for first critical speed predictions: (**a**) SVR-LHS; (**b**) SVR-UD; (**c**) Kriging-LHS; (**d**) Kriging-UD; (**e**) GRU-KAN-LHS; (f) GRU-KAN-UD.

The error distributions are compared in Figure 9. All models exhibit approximately normal error distributions. GAUD sampling shows a smaller interquartile range than

LHS sampling, indicating tighter error concentration and superior predictive performance; GRU-KAN-UD has the smallest range and interquartile spread.

Table 4. Hyperparameter search spaces.

Model	Hyperparameter	Range/Options
GRU-KAN	Batch size	{16, 32, 64, 128}
	Learning rate	$[10^{-4}, 10^{-1}]$
	Hidden dimension	integers $[16, 64]$
	GRU layers	integers $[1, 3]$
SVR	Kernel type	{linear, poly, rbf, sigmoid}
	Regularization strength	$[0.1, 100]$
	Epsilon tube width	$[0.01, 1.0]$
Kriging	Kernel type	{rbf, matern}
	Length scale	$[10^{-3}, 10^{3}]$
	Constant value	$[10^{-3}, 10^{3}]$
	Noise level	$[10^{-10}, 10^{-3}]$

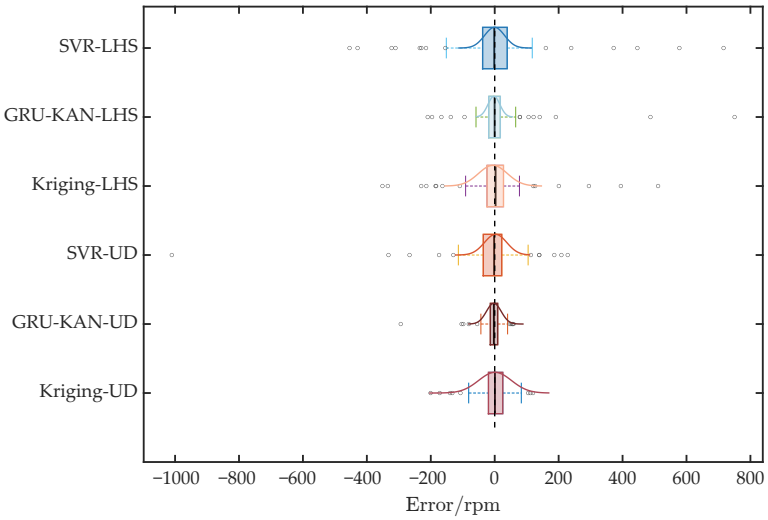


Figure 9. Comparison of error distributions under different models.

For a quantitative evaluation, we compute the following metrics: mean absolute error (E_m), mean absolute percentage error (E_{mp}), mean square error (E_{ms}), and root mean square error (E_{rms}).

$$E_m = \frac{1}{n}\sum_{i=1}^{n}|y_i - \hat{y}_i|, \tag{25}$$

$$E_{mp} = \frac{100\%}{n}\sum_{i=1}^{n}\frac{|y_i - \hat{y}_i|}{y_i}, \tag{26}$$

$$E_{ms} = \frac{1}{n}\sum_{i=1}^{n}(y_i - \hat{y}_i)^2, \tag{27}$$

$$E_{rms} = \sqrt{\frac{1}{n}\sum_{i=1}^{n}(y_i - \hat{y}_i)^2}. \tag{28}$$

The coefficient of determination is

$$R^2 = 1 - \frac{\sum_{i=1}^{n}(y_i - \hat{y}_i)^2}{\sum_{i=1}^{n}(y_i - \bar{y})^2}, \tag{29}$$

where n is the number of samples, y_i the observed value, $\hat{y}_i$ the predicted value, and $\bar{y}$ the sample mean.

The standard deviation is

$$\mathrm{SD} = \sqrt{\frac{1}{N}\sum_{i=1}^{N}(\hat{y}_i - \bar{y})^2}. \tag{30}$$

The evaluation metrics are summarized in Table 5. GRU-KAN-UD delivers the lowest errors and the highest $R^2 = 0.9887$, indicating a highly reliable model (an R^2 above 0.9 denotes strong confidence). Furthermore, its SD most closely matches the actual SD (3.78×10^2 rpm).

Table 5. First critical speed prediction error.

Method	E_m (rpm)	E_{mp} (%)	E_{ms}	E_{rms} (rpm)	R^2	SD (rpm)
SVR-LHS	83.03	3.40×10^{-1}	2.26×10^4	150.31	0.8157	2.96×10^2
SVR-UD	60.21	2.42×10^{-1}	1.61×10^4	126.97	0.8877	3.14×10^2
Kriging-LHS	57.60	2.36×10^{-1}	1.12×10^4	105.77	0.9087	3.31×10^2
Kriging-UD	32.47	1.31×10^{-1}	2.46×10^3	49.58	0.9829	3.63×10^2
GRU-KAN-LHS	43.06	1.78×10^{-1}	1.08×10^4	103.97	0.9118	3.03×10^2
GRU-KAN-UD	22.06	8.88×10^{-2}	1.63×10^3	40.32	0.9887	3.63×10^2

To compare the relative performance across different metrics, we normalize each error measure $E_{i,j}$ (where $j \in \{m, mp, ms, rms\}$ indexes E_m, E_{mp}, E_{ms}, E_{rms} and i, k indexes the model) as

$$E_{nom,i,j} = \frac{\frac{\max_k E_{k,j}}{E_{i,j}}}{\sum_{i=1}^{n} \frac{\max_k E_{k,j}}{E_{i,j}}} \tag{31}$$

and similarly normalize the coefficient of determination:

$$R^2_{nom,i} = \frac{R_i^2}{\sum_{i=1}^{n} R_i^2} \tag{32}$$

The radar chart in Figure 10 visualizes each model's composite performance, with a larger enclosed area indicating better overall metrics. GRU-KAN-UD notably outperforms all others, while SVR-UD's normalized E_m and E_{mp} closely match those of Kriging-LHS, further confirming the advantage of GAUD sampling.

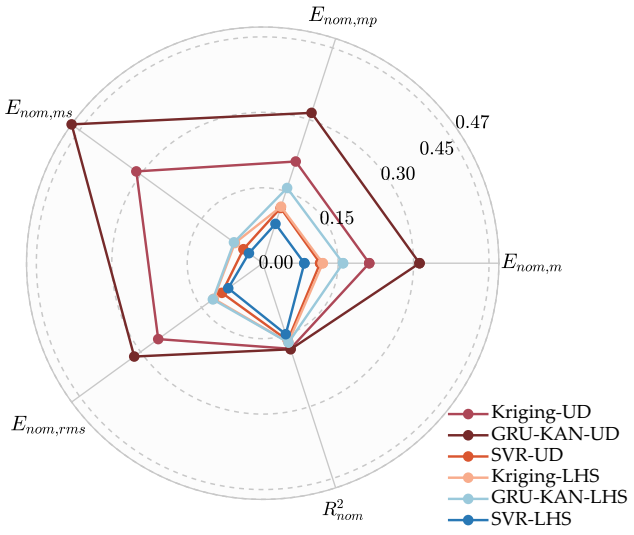


Figure 10. Radar chart of normalized metrics for different models.

3.3. Analysis of Control Parameter Coupling and Critical Speed

Using the GRU-KAN-UD surrogate, we examine the response surfaces of the first critical speed as a function of the bias current I_0 and each control parameter.

Figure 11 shows the surface for (I_0, K_p). As demonstrated in Equations (6) and (7), the parameters k_{xx} and k_{ix} are proportional to I_0^2 and I_0, respectively. The equivalent stiffness $k_e = k_{xx} + k_{ix}\,\mathrm{Re}\{G_c(\cdot)\,G_s(\cdot)\,G_a(\cdot)\}$; thus, both K_p (entering $\mathrm{Re}\{G_c\}$) and I_0 strongly regulate k_e and, in turn, the critical speed. Furthermore, across the full I_0 range, the critical speed decreases monotonically with K_p, with the rate of decline inversely related to I_0. For $K_p \in [2000, 11{,}000]$, the critical speed also decreases monotonically with I_0; for $K_p \in (11{,}000, 20{,}000]$, the response to I_0 is non-monotonic—initially decreasing and then rising. A comparison with Figure 3 reveals that the FEM trends hold only at a specific K_p, demonstrating the surrogate's value in capturing full coupling effects.

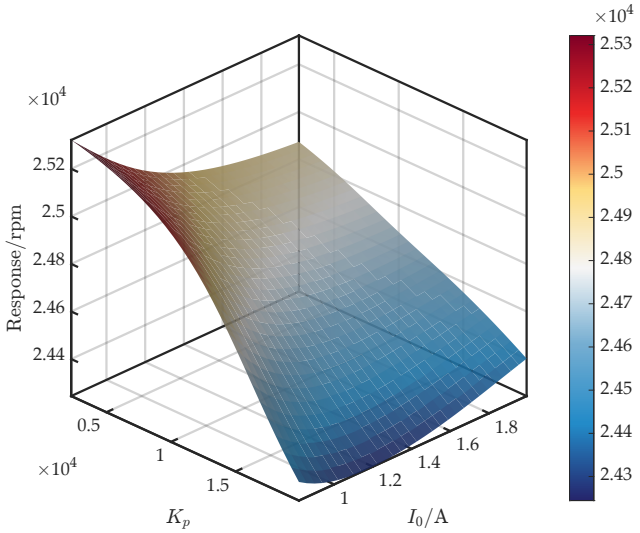


Figure 11. Response surface of first critical speed versus I_0 and K_p.

Figure 12 shows the surface for (I_0, K_i). From Equation (7), K_i contributes mainly at low frequencies to $\mathrm{Im}\{G_c\}$, so its effect on k_e and c_e is limited within the operational bandwidth. Consequently, the influence of K_i on the critical speed is expected to be weak. Furthermore, when $I_0 \in [0.8, 1.3]$, the critical speed decreases monotonically with K_i. For $I_0 \in (1.3, 2]$, the response is non-monotonic: it increases slightly before decreasing.

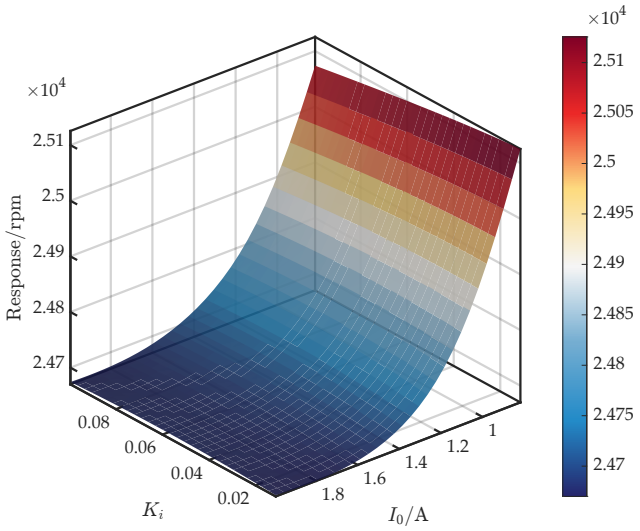


Figure 12. Response surface of first critical speed versus I_0 and K_i.

Figure 13 shows the surface for (I_0, K_d). From Equations (6) and (7), K_d amplifies $\mathrm{Im}\{G_c\}$ in the relevant band, so K_d directly increases c_e, while I_0 scales with k_{ix} and simultaneously affects c_e. Moreover, because I_0 exerts an influence on both k_e and c_e, its net impact on the critical speed is stronger than that of K_d. Accordingly, for $I_0 \in [1.1, 2]$, the critical speed increases with K_d. For $I_0 \in [0.8, 1.1)$, the response is non-monotonic: it rises and then falls.

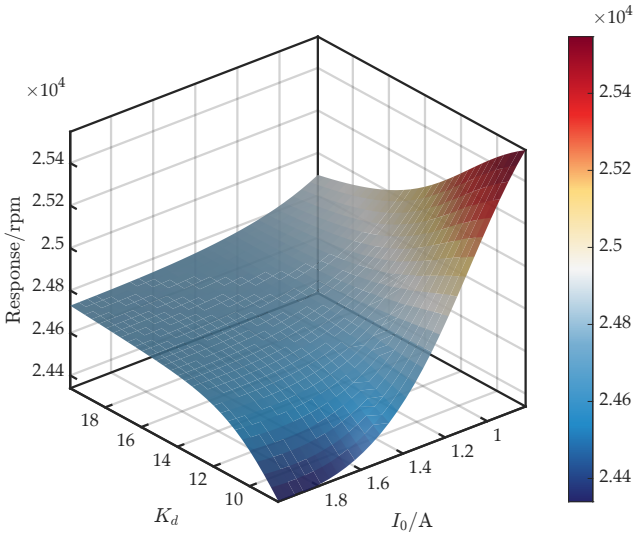


Figure 13. Response surface of first critical speed versus I_0 and K_d.

Figure 14 shows the surface for (I_0, T_d). From Equation (7), T_d exerts a significant influence on the derivative filter, while contributing marginally to k_e and c_e within the operational frequency range; hence, a limited effect on the critical speed is expected. Accordingly, when $I_0 \in [0.8, 1.1]$, the critical speed exhibits a non-monotonic increase and then decrease with T_d. For $I_0 \in (1.1, 2]$, it decreases monotonically as T_d increases.

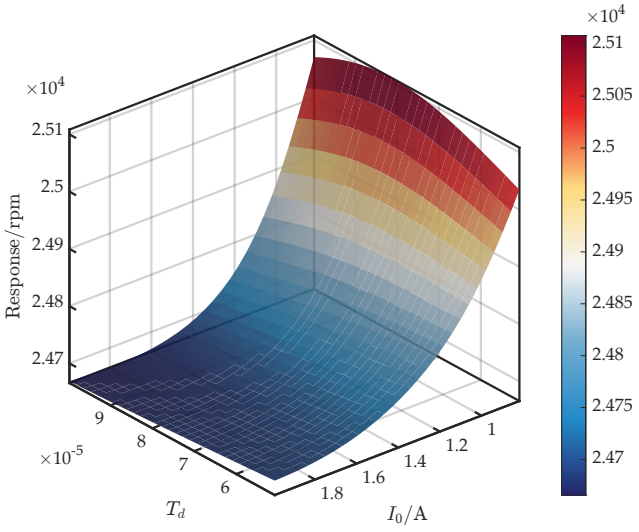


Figure 14. Response surface of first critical speed versus I_0 and T_d.

4. Experimental Validation

An acceleration test was performed to validate the AMB–rotor surrogate model based on GRU-KAN-UD. A PID controller with gains $K_p = 2000$, $K_i = 0.1$, $K_d = 20$, $T_d = 1 \times 10^{-4}$ and bias current $I_0 = 1.4$ A was implemented to maintain stable levitation. The test platform schematic is shown in Figure 15.

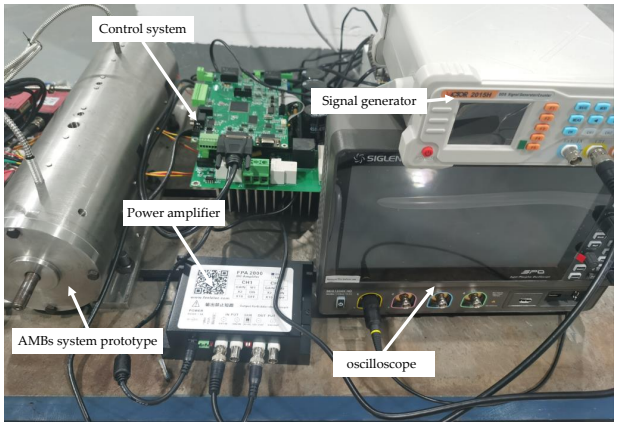


Figure 15. Schematic diagram of the test platform.

Starting from rest, the rotor was accelerated at 60 rpm/s up to 30,000 rpm. The first critical speed was determined to be 24,918.00 rpm from the vibration response during acceleration, as can be seen in Figure 16.

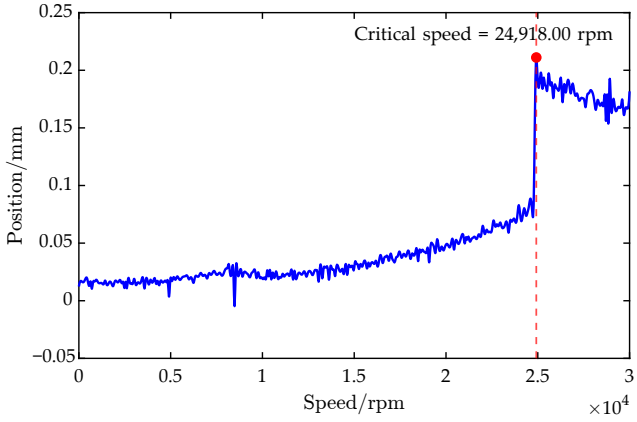


Figure 16. Experimental results of the AMB–rotor vibration responses.

Table 6 compares the first critical speeds obtained from the surrogate model, the FEM, and the experimental measurement. The FEM's prediction deviated from the experiment by 47.46 rpm (1.90×10^{-1} %), confirming its accuracy and providing a solid foundation for surrogate construction. The surrogate model's prediction differed from the experiment by only 51.92 rpm (2.08×10^{-1} %), demonstrating close agreement among the model, simulation, and test.

Table 6. Comparison of the first critical speeds of various models.

Model/Test Type	Critical Speed (rpm)	E_m (rpm)	E_{mp}(%)
GRU-KAN-UD	24,866.08	51.92	2.08×10^{-1}
FEA	24,870.54	47.46	1.90×10^{-1}
Acceleration test	24,918.00	-	-

In terms of computation time, the surrogate evaluation required only 1.14×10^{-4} s versus 201 s for FEM—an improvement of over four orders of magnitude. This indicates that, once trained, the surrogate could rapidly yield key dynamic parameters without further simulation or experiments.

To assess the robustness across control settings, six values of K_p were tested with $I_0 = 1$ A, $K_i = 0.1$, $K_d = 14$, $T_d = 1 \times 10^{-4}$; the results are shown in Figure 17. Similarly, six values of K_d were tested with $I_0 = 1$ A, $K_i = 0.1$, $K_p = 10{,}000$, $T_d = 1 \times 10^{-4}$; the results

appear in Figure 18. Furthermore, six values of I_0 were tested with $K_d = 16$ A, $K_i = 0.1$, $K_p = 15{,}000$, $T_d = 1 \times 10^{-4}$; the results are shown in Figure 19.

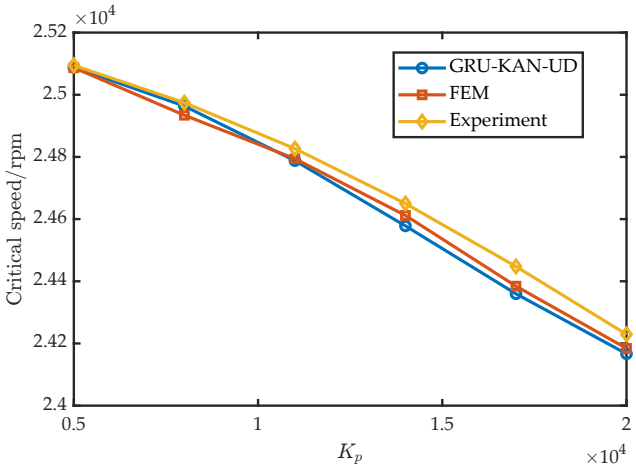


Figure 17. Experimental validation under varying K_p.

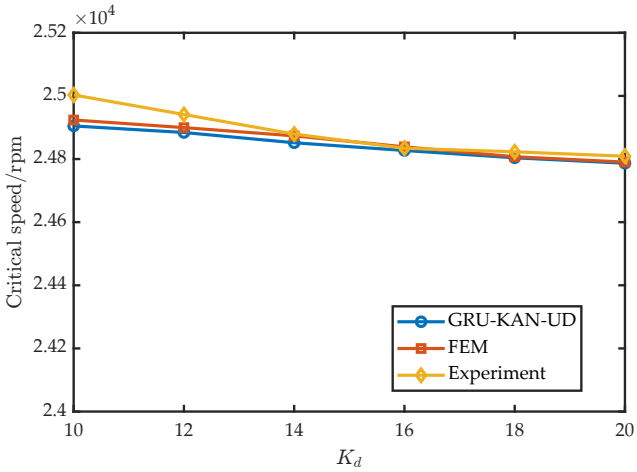


Figure 18. Experimental validation under varying K_d.

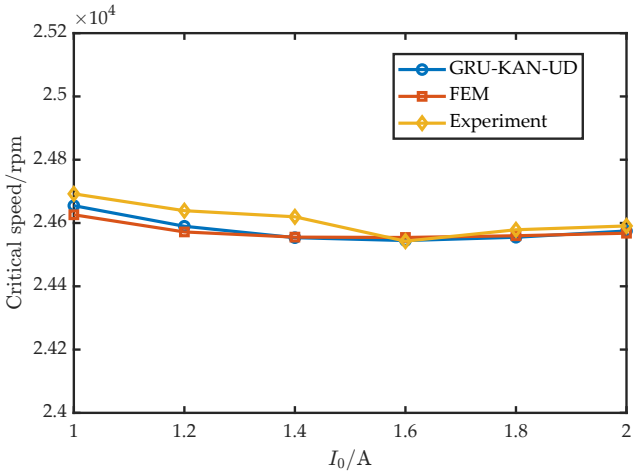


Figure 19. Experimental validation under varying I_0.

Across 18 parameter combinations, the surrogate maintained high accuracy over the design space: relative to the experiment, $E_m = 38.51$ rpm and $E_{mp} = 1.56 \times 10^{-1}$ %; relative to FEM, $E_m = 14.30$ rpm and $E_{mp} = 5.80 \times 10^{-2}$ %.

5. Conclusions

The key findings are as follows:

1. We introduce a surrogate-based method for the analysis of the coupling between the control parameters and the AMB–rotor's first critical speed. The GRU-KAN-UD surrogate achieves a mean absolute error of 38.51 rpm and a mean absolute percentage error of 1.56×10^{-1} %. The experimental results confirm the surrogate's feasibility and precision, providing a solid theoretical and practical foundation for AMB–rotor dynamic modeling.
2. Compared with FEM, the trained surrogate model reduces the computation time from 201 s to 1.14×10^{-4} s while maintaining high fidelity, demonstrating a significant speed advantage.
3. Unlike single-parameter studies, the surrogate approach captures the interaction effects among controller gains, offering a more comprehensive dynamic analysis.
4. We propose a genetic algorithm-enhanced uniform design for sample selection, improving the robustness of surrogate training. The resulting GRU-KAN-UD attains the highest goodness of fit among all candidates ($R^2 = 0.9887$) and the lowest mean absolute error in cross-validation (22.06 rpm), with error reductions of over 60% relative to Kriging-LHS and over 70% relative to SVR-LHS.

The GRU-KAN surrogate is tailored to AMB–rotor dynamics and performs well on the studied configuration. However, its ability to generalize across other fields may be limited. Future work may explore ensemble learning and domain adaptation to enhance the robustness and out-of-domain generalization.

The present study focuses on predicting the critical speed; transient amplitude prediction under time-varying conditions remains to be explored. To broaden the applicability in magnetic bearing rotors, future extensions should incorporate external loads and system condition variations such as temperature rises.

The surrogate provides practical utility for controller pre-tuning and for design space exploration from a rotor dynamics perspective, enabling efficient early-stage assessment without repeated high-fidelity simulations.

Author Contributions: J.C.: writing—original draft, methodology, formal analysis, data curation, conceptualization; J.L.: supervision, conceptualization, project administration, funding acquisition; Z.Z.: methodology, conceptualization; Y.L.: writing—original draft, formal analysis; F.C.: supervision, methodology, conceptualization. All authors have read and agreed to the published version of the manuscript.

Funding: This work is supported by the Shaanxi Provincial Key R&D Program (No. 2023-ZDLGY-17 and No. S2025-YF-ZDXM-CYJQ-0186) and the Xi'an Major Science and Xi'an Science and Technology Program Project (No. 23ZCKCGZH0008).

Institutional Review Board Statement: Not applicable.

Informed Consent Statement: Not applicable.

Data Availability Statement: Data will be made available by the corresponding author on request.

Conflicts of Interest: The authors declare no conflicts of interest.

References

1. Falkowski, K.; Kurnyta-Mazurek, P.; Szolc, T.; Henzel, M. Radial magnetic bearings for rotor–shaft support in electric jet engine. *Energies* **2022**, *15*, 3339. [CrossRef]
2. Wu, T.; Zhang, W. Review on Key Development of Magnetic Bearings. *Machines* **2025**, *13*, 113. [CrossRef]
3. Zhu, Z.; Qi, G.; Xu, J.; Li, X. Dynamic Modeling of the Support System for Vehicle-Mounted Spherical Magnetic Suspension Flywheel Battery. *IEEE Trans. Energy Convers.* **2023**, *39*, 322–333. [CrossRef]

4. Uzhegov, N.; Smirnov, A.; Park, C.H.; Ahn, J.H.; Heikkinen, J.; Pyrhönen, J. Design aspects of high-speed electrical machines with active magnetic bearings for compressor applications. *IEEE Trans. Ind. Electron.* **2017**, *64*, 8427–8436. [CrossRef]
5. Sun, J.; Zhou, H.; Ma, X.; Ju, Z. Study on PID tuning strategy based on dynamic stiffness for radial active magnetic bearing. *ISA Trans.* **2018**, *80*, 458–474. [CrossRef]
6. Wei, Z.; Song, C.; Li, J.; Li, M. Research on vibration characteristics of magnetic suspension bearing-rotor system under variable supporting stiffness. *Bearing* **2022**, *3*, 15–22.
7. Kumar, P.; Tiwari, R. Finite element modelling, analysis and identification using novel trial misalignment approach in an unbalanced and misaligned flexible rotor system levitated by active magnetic bearings. *Mech. Syst. Signal Process.* **2021**, *152*, 107454. [CrossRef]
8. Kumar, P.; Tiwari, R. Dynamic analysis and identification of unbalance and misalignment in a rigid rotor with two offset discs levitated by active magnetic bearings: A novel trial misalignment approach. *Propuls. Power Res.* **2021**, *10*, 58–82. [CrossRef]
9. Mushi, S.E.; Lin, Z.; Allaire, P.E. Design, construction, and modeling of a flexible rotor active magnetic bearing test rig. *IEEE/ASME Trans. Mechatronics* **2011**, *17*, 1170–1182. [CrossRef]
10. van Rensburg, J.J.; Van Schoor, G.; Van Vuuren, P.; van Rensburg, A.J. Non-linear model of rotor delevitation in an active magnetic bearing system including parameter estimation. *Measurement* **2017**, *109*, 256–267. [CrossRef]
11. Sun, J.; Zhou, H.; Ju, Z. Dynamic stiffness analysis and measurement of radial active magnetic bearing in magnetically suspended molecular pump. *Sci. Rep.* **2020**, *10*, 1401. [CrossRef] [PubMed]
12. Chen, Y.; Du, L.; Sun, Q.; Bai, J. A Disturbance Compensation Control Strategy for Rotational Speed Standard Device Based on AMB System. *Sensors* **2024**, *24*, 3093. [CrossRef]
13. Hutterer, M.; Schrödl, M. Modeling and mu-synthesis control of a flexible rotor stabilized by active magnetic bearings including current free control. *J. Sound Vib.* **2023**, *546*, 117439. [CrossRef]
14. Sugimoto, H.; Chiba, A. Dynamic modeling and experimental validations of passing through critical speeds by high acceleration in one-axis actively positioned bearingless motors. *IEEE Trans. Ind. Appl.* **2021**, *57*, 6956–6964. [CrossRef]
15. Shata, A.M.A.H.; Hamdy, R.A.; Abdelkhalik, A.S.; El-Arabawy, I. A fractional order PID control strategy in active magnetic bearing systems. *Alex. Eng. J.* **2018**, *57*, 3985–3993. [CrossRef]
16. Song, X.; Lv, L.; Sun, W.; Zhang, J. A radial basis function-based multi-fidelity surrogate model: Exploring correlation between high-fidelity and low-fidelity models. *Struct. Multidiscip. Optim.* **2019**, *60*, 965–981. [CrossRef]
17. Chelladurai, S.J.S.; Murugan, K.; Ray, A.P.; Upadhyaya, M.; Narasimharaj, V.; Gnanasekaran, S. Optimization of process parameters using response surface methodology: A review. *Mater. Today Proc.* **2021**, *37*, 1301–1304. [CrossRef]
18. Cai, F.; Huang, X. Study on Trajectory Optimization of Hypersonic Vehicle Based on Neural Network. *Front. Energy Res.* **2022**, *10*, 884624. [CrossRef]
19. Sinou, J.J.; Denimal, E. Reliable crack detection in a rotor system with uncertainties via advanced simulation models based on kriging and Polynomial Chaos Expansion. *Eur. J. Mech.-A/Solids* **2022**, *92*, 104451. [CrossRef]
20. Zhou, Z.; Dai, Y.; Wang, G.; Li, S.; Pang, J.; Zhan, S. Thermal displacement prediction model of SVR high-speed motorized spindle based on SA-PSO optimization. *Case Stud. Therm. Eng.* **2022**, *40*, 102551. [CrossRef]
21. Shuai, H.; Li, F. Physics-informed kolmogorov-arnold networks for power system dynamics. *IEEE Open Access J. Power Energy* **2025**, *12*, 46–58. [CrossRef]
22. Tian, J.; Hou, M.; Bian, H.; Li, J. Variable surrogate model-based particle swarm optimization for high-dimensional expensive problems. *Complex Intell. Syst.* **2023**, *9*, 3887–3935. [CrossRef]
23. Bogoclu, C.; Roos, D.; Nestorović, T. Local Latin hypercube refinement for multi-objective design uncertainty optimization. *Appl. Soft Comput.* **2021**, *112*, 107807. [CrossRef]
24. Sheikholeslami, R.; Razavi, S. Progressive Latin Hypercube Sampling: An efficient approach for robust sampling-based analysis of environmental models. *Environ. Model. Softw.* **2017**, *93*, 109–126. [CrossRef]
25. Xiang, B.; Shi, Z.; Wen, T.; Liu, H. Attitude stabilization control of three-axis inertial stabilized platform using magnetically suspension system. *Measurement* **2025**, *253*, 117858. [CrossRef]
26. Kudela, J.; Matousek, R. Recent advances and applications of surrogate models for finite element method computations: A review. *Soft Comput.* **2022**, *26*, 13709–13733. [CrossRef]
27. Han, Z.; Xu, C.; Qiao, J.; Liu, F.; Chi, J.; Meng, G.; Zhang, K.; Song, W. Recent progress of efficient global aerodynamic shape optimization using surrogate-based approach. *Acta Aeronaut. Astronaut. Sin.* **2020**, *41*, 30–70.
28. Lü, Q.; Chan, C.L.; Low, B.K. Probabilistic evaluation of ground-support interaction for deep rock excavation using artificial neural network and uniform design. *Tunn. Undergr. Space Technol.* **2012**, *32*, 1–18. [CrossRef]
29. Cui, J.; Li, J.; Zhao, W.; Zhai, X.; Liu, W.; Chen, C. Research on High Altitude Simulation Test of Aero-engine Based on Genetic Algorithm Optimization Uniform Design. *J. Ordnance Equip. Eng.* **2023**, *44*, 285–289.
30. Gu, J.; Hua, W.; Yu, W.; Zhang, Z.; Zhang, H. Surrogate model-based multiobjective optimization of high-speed PM synchronous machine: Construction and comparison. *IEEE Trans. Transp. Electrif.* **2022**, *9*, 678–688. [CrossRef]

31. Qian, J.; Yi, J.; Cheng, Y.; Liu, J.; Zhou, Q. A sequential constraints updating approach for Kriging surrogate model-assisted engineering optimization design problem. *Eng. Comput.* **2020**, *36*, 993–1009. [CrossRef]
32. Chen, X.; Li, J.; Li, B.; Zou, X.; Cai, F. The multi-stage adding strategy on Kriging and applied to cavitation optimization of centrifugal impeller. *J. Northwestern Polytech. Univ.* **2024**, *42*, 467–476. [CrossRef]
33. Gao, Y.; Hu, Z.; Chen, W.A.; Liu, M.; Ruan, Y. A revolutionary neural network architecture with interpretability and flexibility based on Kolmogorov—Arnold for solar radiation and temperature forecasting. *Appl. Energy* **2025**, *378*, 124844. [CrossRef]

Disclaimer/Publisher's Note: The statements, opinions and data contained in all publications are solely those of the individual author(s) and contributor(s) and not of MDPI and/or the editor(s). MDPI and/or the editor(s) disclaim responsibility for any injury to people or property resulting from any ideas, methods, instructions or products referred to in the content.